Northumbria Research Link

Northumbria University
NEWCASTLE

UniversityLibrary

Mechanical properties of 3D printed architected polymer foams under large deformation

Huan Jiang [a,1], Hannah Ziegler [a,1], Zhennan Zhang [a], Han Meng [b], Dimitrios Chronopoulos [b], Yanyu Chen [a,*]

[a] Department of Mechanical Engineering, University of Louisville, Louisville, KY 40292, USA
[b] Institute for Aerospace Technology & The Composites Group, The University of Nottingham, NG7 2RD, UK

HIGHLIGHTS

- A new type of architected polymer foam composed of spherical shell and beam connector is designed, 3D printed, and tested.
- The architected polymer foam exhibits a bending-dominant behavior with an exponent of 2.2 in the scaling law.
- The stiffness of architected foams can increase about one order of magnitude by tuning the shape of beam connectors.
- The printing process can be used to engineer the deformation pattern and failure modes.

GRAPHICAL ABSTRACT
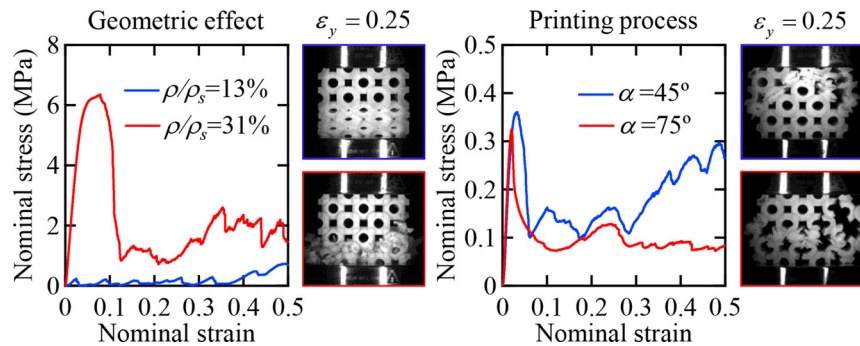
ABSTRACT

We report a new type of three-dimensional architected polymer foams composed of perforated spherical shells and flat strut connectors, which can be precisely produced by 3D printing techniques. We investigate the effects of foam architectures, manufacturing process, and constitutive material on the deformation patterns and failure modes of the proposed architected foams. We demonstrate that flat strut connectors offer unprecedented design flexibility for controlling the mechanical performance. By tuning the geometric parameter of flat strut connectors, the stiffness of architected foams can increase about one order of magnitude while the relative density increases only by 5%. Furthermore, the failure modes can be engineered from a catastrophic one to a progressive one by using weak flat strut connectors. Our experiments elucidate the salient roles of the layer-by-layer manufacturing process and constitutive polymer on the mechanical behavior of the proposed architected foams.

1. Introduction

Continuous efforts are being made to develop lightweight materials with improved stiffness, strength, and energy absorption properties for a variety of multifunctional applications [1–3]. Lightweight materials are characterized by their low density and high strength to weight ratio, making them ideal for aerospace, biomedical, semiconductor, and automotive industries. Foam is a rapidly evolving lightweight structural material, which exhibits high specific strength, exceptional energy absorption, damping, and thermal properties [1,4–10]. Open-cell foams are characterized by the network of interconnected open pores, while closed-cell foams are the combination of individual cells separated by thin membranes [11–15]. Closed-cell foams have underperformed compared to initial predictions due to defects that significantly reduce

mechanical properties [16,17]. In addition, disconnected individual cells also limit their applications. By contrast, open-cell foams have shown favorable mechanical properties under compression [18,19]. Furthermore, the high volume of interconnected porosity and large surface area make open-cell foams attractive in various applications [20–22].

Conventional foams have porosity randomly distributed within the material, taking inspiration from naturally occurring cellular structures such as bone and wood [12]. The internal geometry of random foam is described by relative density and pore size. The most common fabrication method for random metal foam is powder metallurgy [18,23–27]. This technique allows for adjustable pore sizes between 0.3 and 5 mm, and relative densities between 9% and 30%. Additionally, powder metallurgy allows for flexible material selection and is commonly used for steels, titanium, nickel, and copper. However, there are also drawbacks to this method. Bonds between sintered spheres are weak, meaning cutting the desired shape from a sintered slab of material is challenging. It is difficult to achieve complex geometries or smooth edges when cutting specimens [23]. Samples can also be molded into the desired shape before sintering. However, this method decreases sample porosity and alters the shape of hollow spheres, potentially weakening the specimen [25]. Notably, the stochastic nature of these random foams could degrade mechanical performance in uncontrollable ways.

Architected materials with well-defined structures can be exploited to achieve tailored and unprecedented mechanical properties and functionalities. Two-dimensional (2D) and two-dimensional (3D) architected materials have been produced by using additive manufacturing to explore the effect of unit cell geometry and connectivity on mechanical performance [28–34]. For example, numerical and experimental studies found that hybrid honeycomb structures possessed superior energy absorption compared to traditional honeycombs. Coupling between failure of the two lattice designs and localized fracture resulted in sustained plateau stress for increased energy absorption [31]. Means of tailoring mechanical performance outside of the traditional method of varying relative density have also been explored for optimizing architected polymer structures without increasing weight. For example, higher stiffness was observed in 3D printed polymeric periodic structures using selective wall thickening in high-stress regions to delay collapse. Additionally, it was found that varying porosity can change the deformation mode from bending to stretch-dominant, resulting in a more favorable structure [29]. Base material selection has also been explored for controlling deformation mode and mechanical properties of octet truss lattices. It was found that a more rigid polymer will produce a stiffer structure with stretch-dominant behavior, while a more compliant polymer will tend toward bending-dominant due to lower solid material properties [35]. Nodal connectivity has been used as another means of controlling the performance of additively manufactured polymer structures without significantly affecting weight [30,36]. It was found that pin joints and spherical joints, while similar in relative density and elastic behavior, can be selected to produce stretch-dominant and bending-dominant tensegrity-inspired structures, respectively. More recently, filled 3D printed flexible polymer lattice structures have been devised for tailored energy absorption with shape recovery by controlling internal pressure [37]. Architected polymer foams (APFs) is another type of architected materials that has gained increasing attention recently. Geometric control in APF facilitates tailored and simultaneous vibroacoustic control [38,39]. APFs have also demonstrated more efficient energy absorption than metal foams and have shown an ability to recover their initial shape after large deformation [40]. Despite these design flexibilities and advanced manufacturing techniques, studies on mechanical response of architected foams under large deformation are quite limited.

In this work, the mechanical response of 3D printed APFs under large deformation is studied. By subjecting the polymer architecture to large compressive strains (70%), this research determines the energy absorption of the foams as well as elastic properties. Geometric parameters, manufacturing process, and constitutive material are found to have significant effects on mechanical properties, deformation patterns, and failure modes of the architected foams.

2. Materials and methods

2.1. Model design and 3D printing

The proposed APF with a body-centered cubic (BCC) lattice symmetry consists of perforated spherical shells and flat strut connectors (Fig. 1 (a) and (b)). The lattice constant of the representative volume element (RVE) is a. Fig. 1 (c) shows the one-eighth of the RVE. Perforated spherical shell is characterized by external radius R, thickness t, and perforation radius r. Flat strut connector is described by length l, height h, and fillet radius b, or a single parameter, binder angle θ. The binder angle θ is schematically shown in Fig. 1(c). In our design, the length, l, height h, and fillet radius b can be equivalently expressed by R and θ. The relative density of the proposed APF can be calculated as

$$
\begin{aligned}
\frac{\rho}{\rho_s} = & \left(\frac{6\sqrt{3}}{25}\right)^3 \left\{ \frac{168\sqrt{21}\pi}{125} - 8\pi\left[\frac{21}{25} - \frac{2t}{R} + \left(\frac{t}{R}\right)^2\right]^{\frac{3}{2}} \right. \\
& - \frac{16\pi}{3}\left[\frac{3t}{R} - 3\left(\frac{t}{R}\right)^2 + \left(\frac{t}{R}\right)^3\right] + \frac{2\pi}{3}\left(\frac{25}{24}\tan\theta + 1 - \frac{25}{24\cos\theta}\right)^2 \right\} \\
& + c\left(\frac{t}{R}\right)^3
\end{aligned}
\tag{1}
$$

where the relation between R and a is assumed as $R = 6\sqrt{3}a/25$. The radius of the perforation is set as $r = 2R/5$. The binder correction coefficient is defined as the correction of the volume of binder because the binder volume cannot be calculated analytically. We calculate $\pi h^2 l/4$ as the first part of binder volume, then use the binder correction coefficient to correct the rest. $c = 0.027$ is determined by fitting Eq. (1) from CAD calculations. By changing the spherical thickness t, one can change the relative density. By changing the binder angle θ, one can tailor the shape of flat strut connectors, thereby changing the connectivity among the spherical shells. In this work, the lattice constant is set as $a = 25$ mm.

All samples were 3D printed using Objet260 Connex3 printer (Stratasys, USA), with a printing resolution of 16 μm [41,42]. RGD515/531 was chosen as the base material because it is a ductile polymer material in the printer. Printing angle is denoted as α and defined as the angle between the build layers and load direction. To vary the printing direction, samples were rotated to achieve the desired angle relative to the build tray. Once the samples were removed from the build tray, support material was carefully removed by using waterjet (Stratasys, USA). After that, a mixed solution of sodium hydroxide and sodium metasilicate was prepared in Branson ultrasonic cleaner (Emerson Electric, USA) to dissolve the remaining support material on the concave side of shells. Printed samples with different relative densities and binder angles are shown in Fig. 1 (d) and (e), respectively.

2.2. Mechanical testing

Two sets of compression experiments were conducted to determine the impact of geometric parameters, shell thickness and binder angle, on mechanical performance. The effects of 3D printing direction and strain rate on mechanical performance were also tested. Specimens were uniaxially compressed by Instron 5569A mechanical tester (Instron, USA) [43]. Load direction was perpendicular to 3D printed layers for geometry and strain rate testing. Unless otherwise specified, the compressive extension rate was 2.25 mm/min, corresponding to a compressive strain rate $5 \times 10^{-4} s^{-1}$. Specimens were loaded until 70% deformation. Specific energy absorption was approximated using midpoint numerical integration as the area under the stress-strain

curve, up to maximum deformation of 70% strain. Prior to testing, 2D Digital Image Correlation (Correlated Solutions, USA) equipment was installed to capture deformation patterns and failure modes.

2.3. Finite element simulations

Finite element simulations were performed to provide additional insights into the deformation mechanisms of the APFs. The dynamic explicit solver with adaptive time-stepping was employed. Two sets of models with different binder angles and relative densities were simulated. The geometrical models were meshed with first-order hexahedral and second-order tetrahedral elements. The models with binder angles of 10° and 30° were meshed with 202,000 and 274,000 C3D8 elements, respectively. The model of relative density $\rho/\rho_s = 0.13$ was meshed with 217,000 C3D8 elements, and the model with relative density $\rho/\rho_s = 0.31$ was meshed with 866,000 C3D10 elements. Mesh convergence tests were performed to ensure that the number of elements is enough to capture mechanical response. The bottom face was constrained in the vertical direction. The top face was applied compressive displacement of 7.5 mm, corresponding to the strain of 0.1.

A user-defined viscoplastic constitutive model was first developed to simulate the response of the 3D printed polymer in [44], where the detailed description of implementation was given. In addition, reference [45] also adopted this model and made it publicly available. In this paper, we referred to [45] for this constitutive model. The strain energy potential for the Arruda-Boyce model is [46]

$$W = \mu \left\{ \frac{1}{2}\left(\bar{I}_1 - 3\right) + \frac{1}{20\lambda_L^2}\left(\bar{I}_1^2 - 9\right) + \frac{11}{1050\lambda_L^4}\left(\bar{I}_1^3 - 27\right) + \frac{19}{7000\lambda_L^6}\left(\bar{I}_1^4 - 81\right) + \frac{519}{673750\lambda_L^8}\left(\bar{I}_1^5 - 243\right) + \frac{K_0}{2}\left(\frac{J_e^2 - 1}{2} - \ln J_e\right) \right\}$$

(2)

where μ is the initial shear modulus, λ_L is the limiting network stretch, K_0 is the initial bulk modulus, J_e is the elastic volume ratio related to temperature. $\bar{I}_1$ is defined as [47]

$$\bar{I}_1 = I_1 J^{-2/3}$$

(3)

$$I_1 = trace(\boldsymbol{B}) = B_{11} + B_{22} + B_{33}$$

(4)

where $\boldsymbol{B}$ is left Cauchy-Green deformation tensor. The total volumetric ratio J can be described as

$$J = \sqrt{\det(\boldsymbol{B})}$$

(5)

If thermal effect is not considered, $J_e = J$.

The effective shear strain rate can be determined through equation [46]

$$\dot{\gamma}^p = \gamma_0 \exp\left[-\frac{\Delta G}{\kappa\Theta}\left(1 - \left(\frac{\sigma_e}{s}\right)^{5/6}\right)\right]$$

(6)

where γ_0 is the pre-exponential shear strain rate, s is the thermal shear yield strength, κ is the Boltzmann's constant, σ_e is the effective stress, ΔG is the initial free energy change.

The rate of shear yield strength for strain-softening is determined through [46]

$$\dot{s} = h\left(1 - \frac{s}{s_s}\right)\dot{\gamma}^p$$

(7)

where s_s is s at steady state, h is the slope of the strain-softening zone. All the parameters of this user-defined constitutive model are summarized in Table 1. Note that material failure was not considered in all simulations.

3. Results and discussion

3.1. Effect of relative density

Stress-strain curves for relative densities $\rho/\rho_s = 13\%$, 16%, 20%, 25%, and 31% are shown in Fig. 2 (a). Small deformation response including the elastic region and the first peak stress of each sample is shown in Fig. 2 (b) for clarity. Each stress-strain curve shows an initial peak, corresponding to the first failure of each structure. Following the first failure, stress reduces, and compression continues. Stress then increases until another failure occurs. This failure process continues, as evidenced by multiple peaks in the stress-strain curves until all spheres fracture. The remaining material is then compressed upon itself, known as densification, which corresponds to an increase in stress at large strain.

Fig. 2 (c)-(d) show contrasting deformation patterns for relative density $\rho/\rho_s = 13\%$ and $\rho/\rho_s = 31\%$, respectively. Deformation of $\rho/\rho_s = 13\%$ shows a progressive, layer by layer failure. Sequenced failure of layers is also visible in the stress-strain curve, with a peak corresponding to each failed layer. Following the failure of all layers, the structure is compressed further, and the densification begins, corresponding to the rise in the stress-strain curve around $\varepsilon_y = 0.55$. By contrast, the sample with $\rho/\rho_s = 31\%$ shows catastrophic failure. Stress-strain curve for $\rho/\rho_s = 31\%$ is jagged between $\varepsilon_y = 0.1$ and 0.6, with more extreme and less defined peaks compared to $\rho/\rho_s = 13\%$. For $\rho/\rho_s = 13\%$, first layer failure occurs at $\varepsilon_y = 0.025$, corresponding to

yield stress of 0.228 MPa. For $\rho/\rho_s = 31\%$, the first failure occurs much later, at $\varepsilon_y = 0.079$ and yield stress of 6.35 MPa. This can be verified from the second image. When $\varepsilon_y = 0.03$, the bottom layer completely failed for $\rho/\rho_s = 13\%$, while for $\rho/\rho_s = 31\%$ structural integrity is maintained. This is because when thickness increased, the specimen tends to exhibit brittle behavior, which will absorb more energy in the initial stage. As the strain increases to 0.65, the specimen with a relative density of 31% collapses while specimen of 13% still shows structural integrity. This phenomenon can be attributed to the progressive failure mode. By contrast, the model of 31% experiences a catastrophic failure mode during compression.

The mechanical properties, including stiffness, strength, and energy absorption for the APFS, are summarized in Fig. 3. Stiffness is plotted against relative density on a log-log scale and fitted with a power curve (Fig. 3(a)). It is found that relative stiffness is related to relative density by an exponent of 2.2, indicating a bending-dominant deformation behavior. This implies that, for this architecture, varying relative density is inefficient for controlling stiffness. It should be pointed that due to the resolution of the printer, we are unable to print the structures with relative density under 12%. Nevertheless, our designed structures show comparable stiffness with other architected polymer foams [36,48,49], and superior to stochastic polymer foam at high relative density [41]. Yield strength and energy absorption are shown in Fig. 3 (b) and (c), respectively. As expected, strength and energy absorption increase with the relative density.

Fig. 4 shows the simulation results for APFs with $\rho/\rho_s = 13\%$ and $\rho/\rho_s = 31\%$ from $\varepsilon_y = 0$ to 0.1. For $\rho/\rho_s = 13\%$, there is no apparent peaks in the stress-strain curves, meaning this APF experiences a more stable deformation (Fig. 4 (a)). However, for $\rho/\rho_s = 31\%$, the presence of the distinct peak in the stress-strain curve, corresponding to the uniform deformation (Fig. 4 (e)). At the strain of 0.01, simulation contour plot reveals that stresses are concentrated on the spheres around the binders
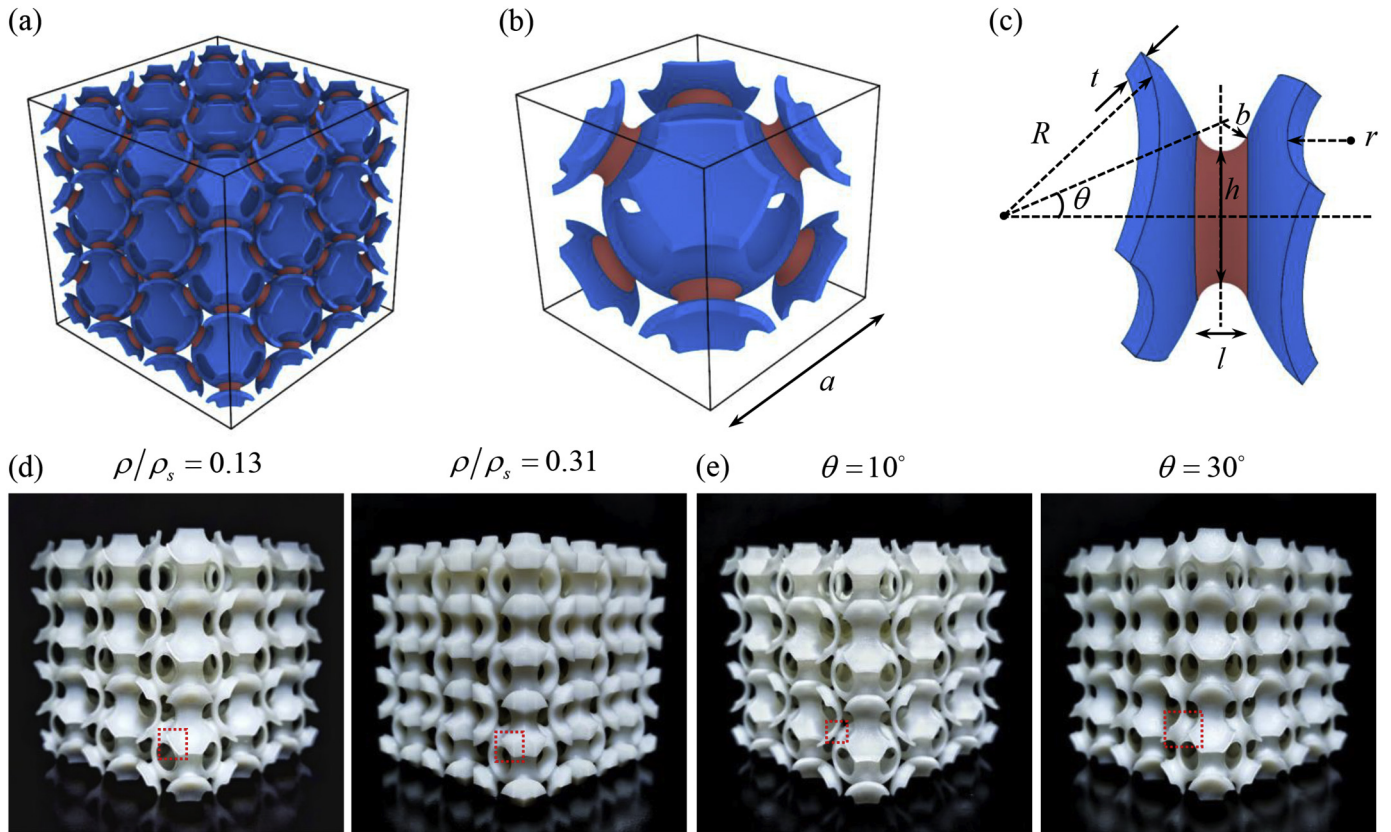
Fig. 1. Design and 3D printing of 3D APFs. (a) APF foam with $3 \times 3 \times 3$ representative volume elements (RVEs). (b) An RVE of APF. The lattice constant of the RVE is a. (c) Detailed geometric parameters for perforated spherical shell and flat strut connector. Sphere radius R, sphere thickness t, perforation radius r, binder parameter θ, and fillet radius b. (d) 3D printed samples with $\rho/\rho_s = 0.13$ and $\rho/\rho_s = 0.31$. Here $a = 25$mm, $r = 4t$, and $\theta = 20$. (e) 3D printed samples with $\theta = 10°$ and $\theta = 30°$. Here $a = 25$mm, $t/R = 1/10$, and $r = 4t$. The dashed squares in (d) and (e) highlight the sphere thickness and size of flat strut connector, respectively.

for $\rho/\rho_s = 13\%$, which leads to the yield of spheres first (Fig. 4 (b)). While for $\rho/\rho_s = 31\%$, much of the stresses concentrate on the binder. This indicates the first yield of binders (Fig. 4 (f)). When $\varepsilon_y = 0.03$, the stresses spread to the spheres, and the spheres in the middle layer exhibit buckling for $\rho/\rho_s = 13\%$ (Fig. 4 (c)). However, for $\rho/\rho_s = 31\%$, the stresses rapidly spread to most of the model and maintain a much higher stress level than that of $\rho/\rho_s = 13\%$ (Fig. 4 (g)). At the strain of 0.08, the stresses remain fairly similar to that of $\varepsilon_y = 0.03$ for $\rho/\rho_s = 13\%$. The spheres show increased buckling, indicating a progressive deformation pattern (Fig. 4 (d)). For $\rho/\rho_s = 31\%$, one however cannot observe localized deformation at this stage. Instead, one can see the shear deformation of binders (Fig. 4 (h)). This indicates that the failure of binders drives the structure to catastrophic collapse, as confirmed by the experiment (Fig. 2 (d)).

Table 1
Parameters for the user-defined constitutive model.

Material parameters	Values
E(MPa)	1200
ν	0.33
γ_0	5.0×10^5
$\Delta G(J)$	1.25×10^{-19}
s(MPa)	70
s_s(MPa)	30
h(MPa)	200
μ(MPa)	4.5
λ_L	3.5

3.2. Effect of binder angle

Stress-strain curves for samples with binder angles of 10°, 20°, and 30° are shown in Fig. 5 (a). Each stress-strain curve shows an initial peak corresponding to the first failure. Stresses rise and fall for each subsequent failure. Failure continues until all spheres or binders fracture, and then densification begins. Young's modulus and energy absorption are shown in Fig. 5 (b) and 5 (c), respectively. By increasing binder angle from $\theta = 10°$ to $\theta = 30°$, stiffness increases over an order of magnitude, while relative density only increases by 5%. With the ability to vastly increase stiffness without greatly increasing weight, binder angle is much more efficient for improving mechanical properties than wall thickness.

Fig. 5 (d)-(e) shows contrasting deformation patterns for binder angles 10° and 30°, respectively. Deformation of $\theta = 10°$ shows progressive failure, which can be observed from Fig. 5 (d), similar to $\rho/\rho_s = 0.13$ at $\theta = 20°$ in Fig. 2 (c). Following layer by layer failure, densification gradually starts around $\varepsilon_y = 0.6$. For $\theta = 30°$, the structure, however, experiences a catastrophic failure. The stress-strain curve shows less defined peaks after $\varepsilon_y = 0.2$, as evidenced by non-uniform deformation in images of $\varepsilon_y = 0.25$ to 0.65. The first failure of $\theta = 10°$ occurs at $\varepsilon_y = 0.039$ with a yield stress of 0.075 MPa. By contrast, the first failure of $\theta = 30°$ begins much earlier. This can be observed from the second image of Fig. 5 (d) and (e) where the bottom layer of $\theta = 30°$ fails at $\varepsilon_y = 0.024$, while $\theta = 10°$ remains intact.

Fig. 6 shows the numerical simulation results for APFs with $\theta = 10°$ and $\theta = 30°$, respectively. We have calibrated our simulation for the model with a relative density of 13%. The calibration reveals that the simulation result is consistent with the experiment for the printing direction 90° while higher than the printing direction of 0°. This is because the mechanical behavior is dependent on printing direction and the
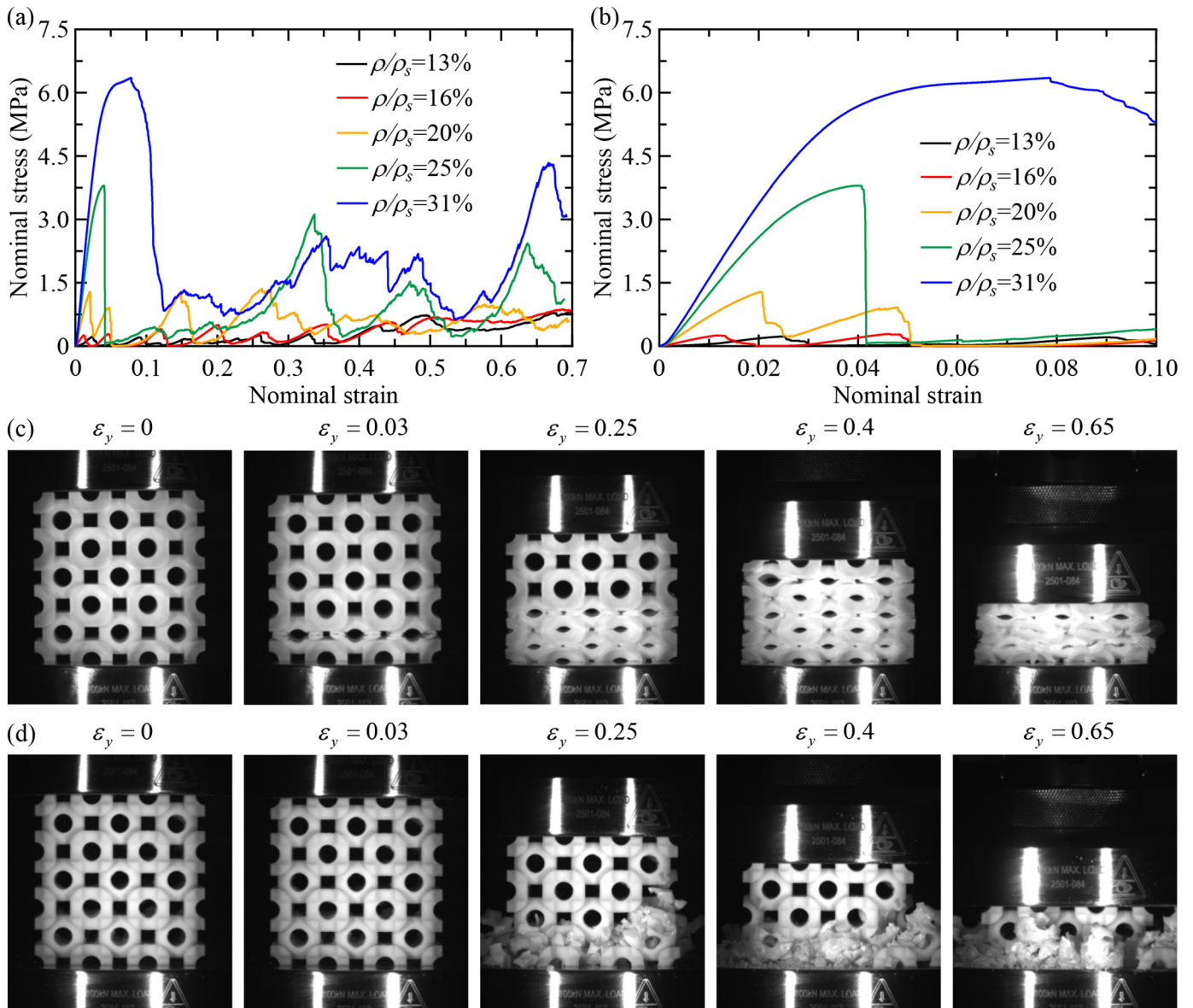
Fig. 2. Effect of relative density on mechanical performance. (a)-(b) Stress-strain relations for different relative densities. (c) and (d) Deformation patterns for $\rho/\rho_s = 0.13$ and $\rho/\rho_s = 0.31$, respectively. Here $a = 25mm, r = 4t, \theta = 20°$.

possible imperfections involved during printing. However, the anisotropic feature and failure are not incorporated in our simulations. It should be noted that the purpose of the numerical simulation in this work is to provide additional information to identify the deformation mechanisms. For $\theta = 10°$, there is no distinct peak on the stress-strain curve, indicating a stable deformation (Fig. 6 (a)). By contrast, the presence of apparent stress peak for $\theta = 30°$ indicates a less uniform deformation (Fig. 6 (e)). At the strain of 0.01, it can be observed that the stresses concentrate on the binders and part of the spheres around binders for $\theta = 10°$ (Fig. 6 (b)). For $\theta = 30°$, the stresses concentrate on local spheres around the binders and the stress level is higher than that of $\theta = 10°$ (Fig. 6 (f)). When $\varepsilon_y = 0.024$, stresses locally concentrate on the interface of different layers for $\theta = 10°$. This leads to yield and buckling of spheres in the middle layer (Fig. 6 (c)). However, for $\theta = 30°$, the stresses spread to most of the model from $\varepsilon_y = 0.01$ to 0.024. This indicates that binder of $\theta = 30°$ functions much more efficiently to transfer stresses from binder to sphere compared with $\theta = 10°$. The high-stress transfer efficiency means that a more uniform stress distribution can be expected for $\theta = 30°$ (Fig. 6 (g)). The uniform stress

distribution drives the APF to a catastrophic failure mode, as confirmed from experiment (Fig. 5 (e)).

3.3. Effect of printing direction

Stress-strain curves for samples printed at $\alpha=0°, 15°, 30°, 45°, 60°, 75°$ and $90°$ are shown in Fig. 7 (a). For clarity, stress-strain curves at small deformation are in Fig. 7 (b). Fig. 7 (c)-(e) show deformation patterns for $\alpha = 15°$, $\alpha = 45°$, and $\alpha = 75°$, respectively. Sample of $\alpha = 15°$ shows progressive failure. The first failure occurs along the printing direction at $\varepsilon_y = 0.027$. Failure begins at the top of the structure at $\varepsilon_y = 0.15$, and propagates along the printing direction. This is expected due to the comparatively weak bonding interface during the layer-by-layer fabrication. Then, failure occurs in other layers, but not sequentially. Finally, well-defined densification can be observed at $\varepsilon_y = 0.6$. By contrast, for $\alpha = 45°$ and $\alpha = 75°$, much more pronounced effect of printing direction can be observed. The first failure occurs at $\varepsilon_y = 0.033$ and $\varepsilon_y = 0.017$ for $\alpha = 45°$ and $\alpha = 75°$, respectively. At $\varepsilon_y = 0.05$, both models exhibit apparent fractures along the printing
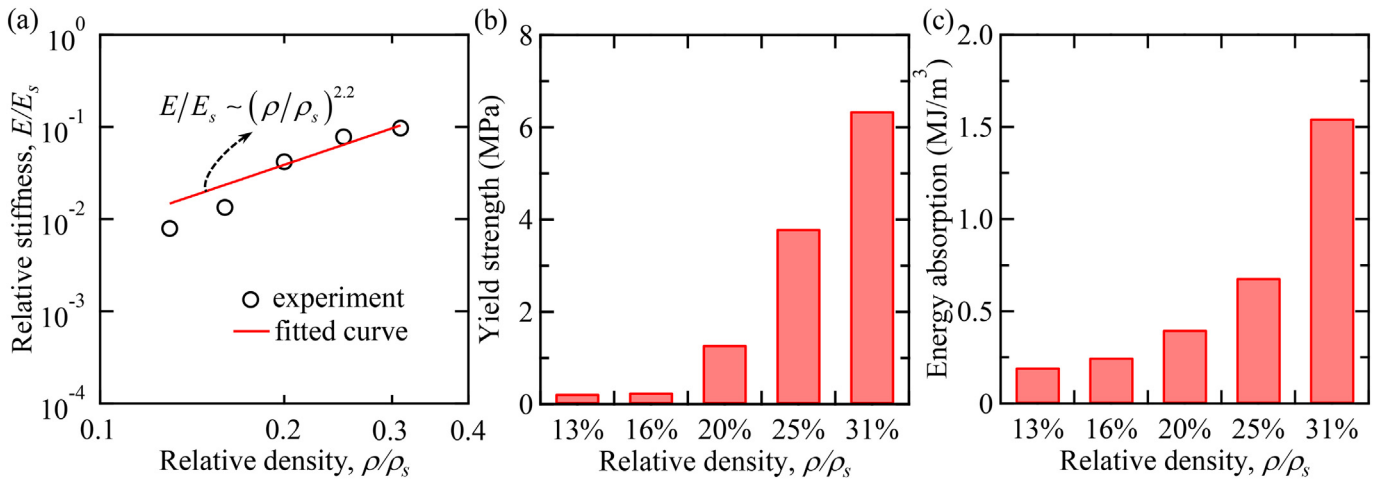
Fig. 3. Effect of relative density on mechanical performance. (a) Stiffness as a function of ρ/ρ_s. (b) Strength as a function of ρ/ρ_s. (c) Energy absorption as a function of ρ/ρ_s. Here $a = 25$mm, $r = 4t$, $\theta = 20°$.

direction, especially for $\alpha = 75°$. When compressed to the $\varepsilon_y = 0.15$, sample of $\alpha = 45°$ shows a clear shear band of $45°$, followed by the failure along with the shear band. After the shear band fails, the remaining part is compressed until the end of the experiment. For $\alpha = 75°$, one cannot observe the shear band as distinct as $\alpha = 45°$ at $\varepsilon_y = 0.15$. However, some parts of the spheres break until disconnected along $75°$. As a result, samples collapse, and no significant densification can be observed at $\varepsilon_y = 0.6$ for these two cases. Intrinsically, this is attributed to

the weak bonding of the interfaces produced during the manufacturing process.

Fig. 8 (a)-(c) show Young's modulus, yield strength, and energy absorption of APFs for different printing directions, respectively. It is shown that the stiffness and strength increase with the printing angle. From a heuristic point of view, composite ply theory can be applied to explain this phenomenon. When loads are parallel to the fibers, the ply is much stronger and stiffer than when loads are transverse to the
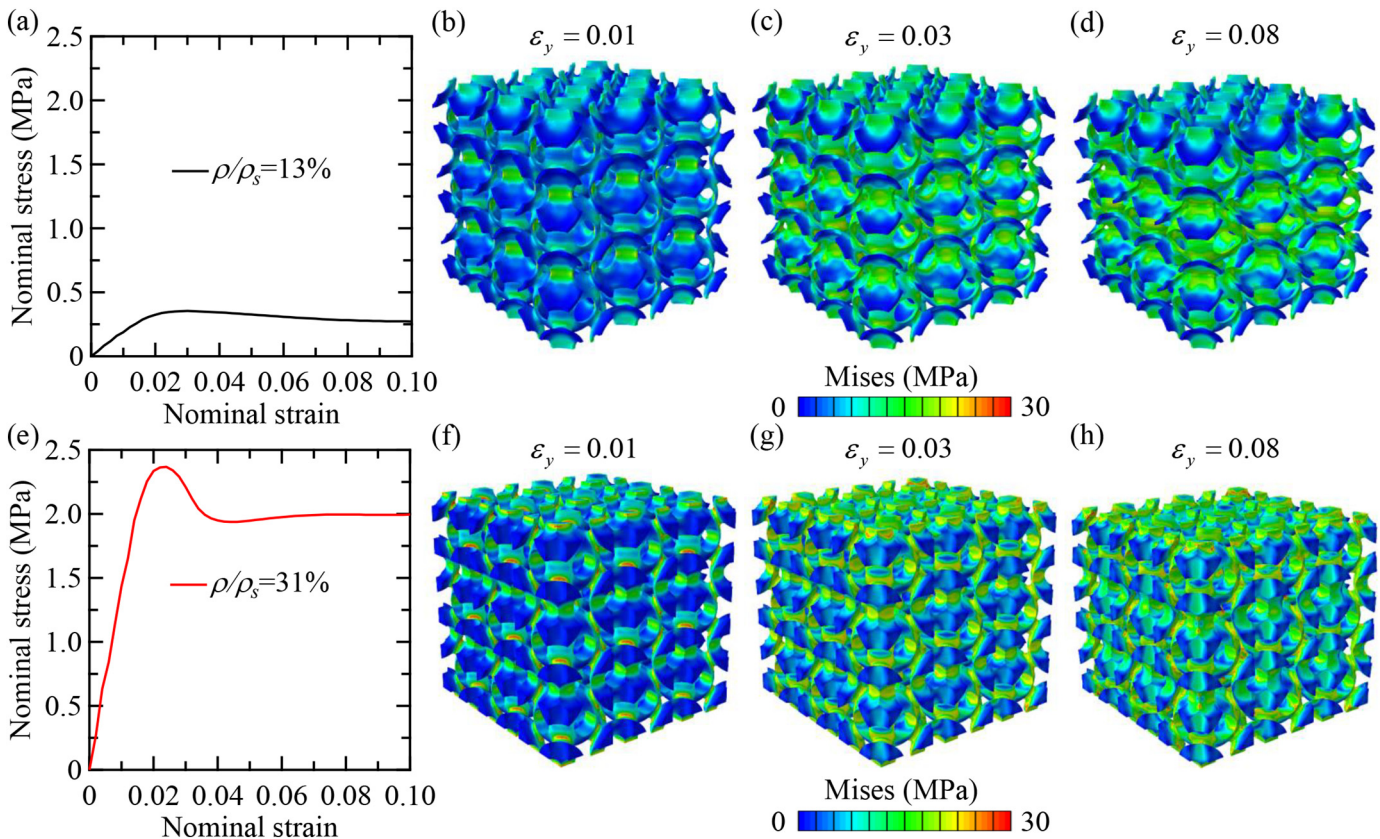

Fig. 4. Finite element simulations for the mechanical response of APFs with different relative densities. (a) Simulated stress-strain curve for $\rho/\rho_s = 0.13$. (b)-(d) Simulated deformation patterns for $\rho/\rho_s = 0.13$. (e) Simulated stress-strain curve for $\rho/\rho_s = 0.31$. (f)-(h) Simulated deformation patterns for $\rho/\rho_s = 0.31$.

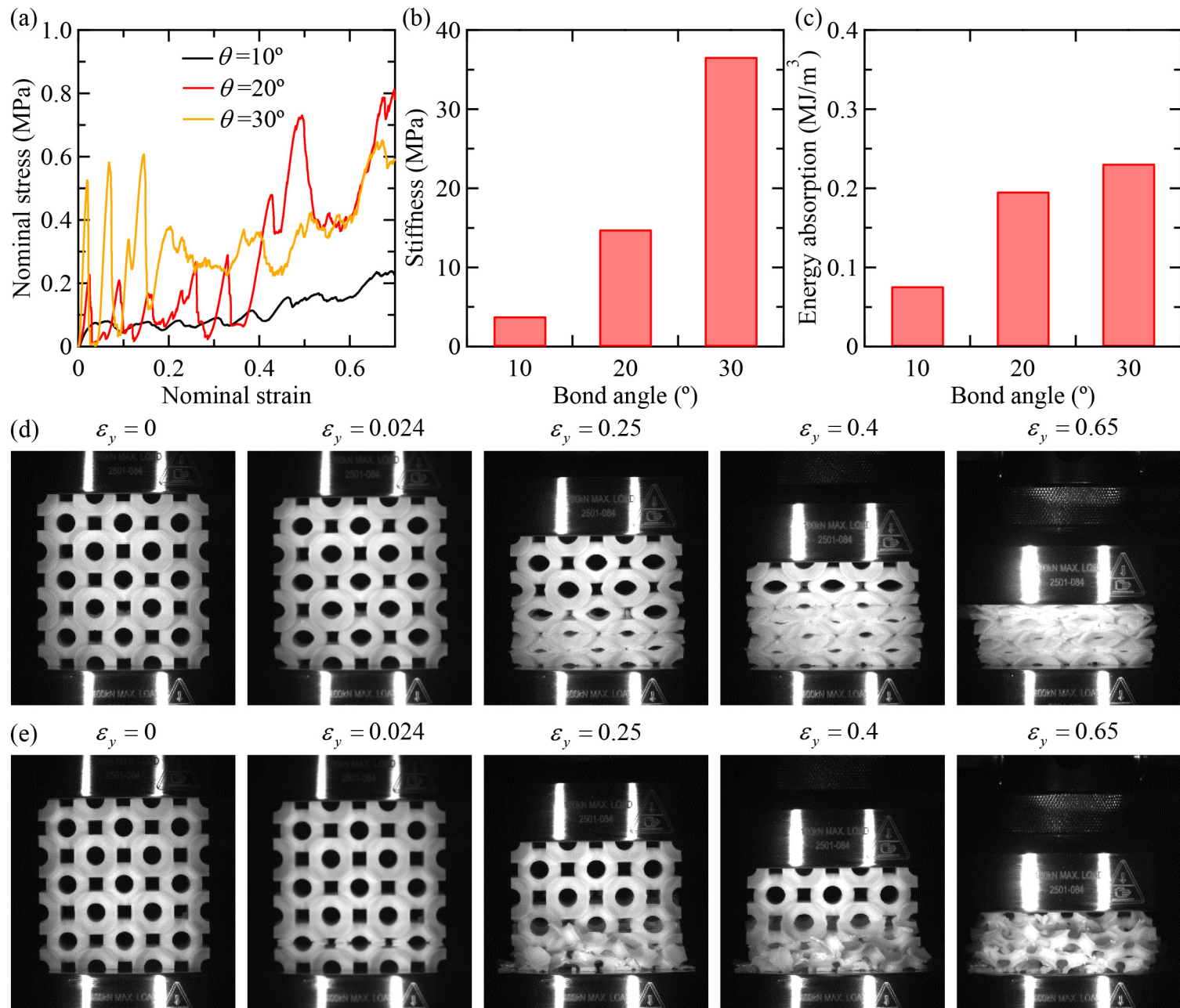**Fig. 5.** Effect of binder angle on mechanical performance. (a) Stress-strain relations for $\theta = 10°$, $\theta = 20°$, and $\theta = 30°$. (b) Stiffness. (c) Energy absorption. (d) and (e) Deformation patterns for $\theta = 10°$ and $\theta = 30°$, respectively. Here $a = 25$mm, $\rho/\rho_s = 0.13$, $r = 4t$.
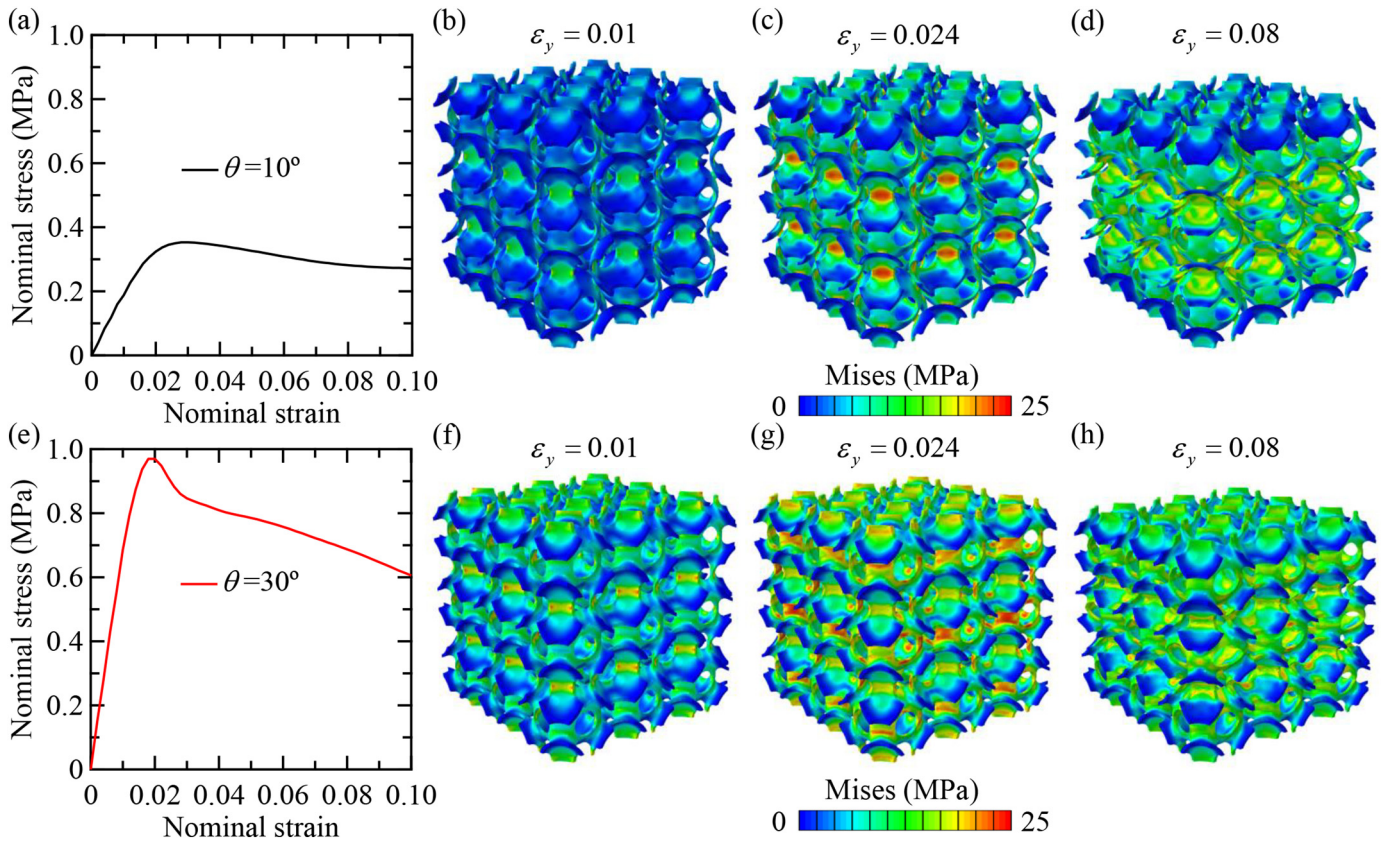
Fig. 6. Finite element simulations for the mechanical response of APFs with different binder angles. (a) Simulated stress-strain curve for $\theta = 10°$. (b)-(d) Simulated deformation patterns for $\theta = 10°$. (e) Simulated stress-strain curve for $\theta = 30°$. (f)-(h) Simulated deformation patterns for $\theta = 30°$.

fiber direction. By analogizing the printed layers to fibers, one can explain the increasing trend of stiffness with the printing direction. Energy absorption is highest for $\alpha = 15°$ and decreases with increasing α, as failure becomes less stable, until $\alpha = 90°$.

3.4. Effect of loading rate

Depending on the applications of APFs, the structure could be subjected to different loading rates. Five strain rates were tested on the same geometry to understand the effect of loading rate on the mechanical response. Stress-strain curves for samples subjected to strain rates 0.1, 0.01, 0.001, 0.0005, and 0.00001 s^{-1} are shown in Fig. 9 (a). Stress-strain curves at small deformation are shown in Fig. 9 (b). Multiple peaks exist for all stress-strain curves, corresponding to a layer-by-layer failure mode. Notably, peaks become increasingly less as the strain rate increases. Deformation continues in each structure until all spheres break, followed by densification. Fig. 9 (c) and (d) show deformation patterns for strain rate of 0.1 and 0.00001 s^{-1}, respectively. Deformation at a strain rate of 0.1 s^{-1} shows a non-uniform and catastrophic failure. The first failure occurs at $\varepsilon_y = 0.03$, corresponding to yield stress of 0.645 MPa. Failure begins in the middle layer of the specimen. Initial failure is less uniform throughout the layer than other stable layer failures, resulting in the loss of small fragments. At $\varepsilon_y = 0.07$, the failed layer is compressed until another failure occurs due to insufficient time to further absorb energy. At $\varepsilon_y = 0.14$, the second failure is not contained within one layer of the structure but spans multiple layers surrounding the first failed layer. Collapsed spheres create a shear deformation band from the bottom left corner of the specimen to the middle right. Partial failure of layers results in the continued non-uniform collapse. The polymer is contained within the initial profile and the top layer has not fractured for $\varepsilon_y = 0.22$. The APF compressed at the

strain rate of 0.00001 s^{-1}, however, shows a stable and progressive failure mode. Different from the fragmented collapse of the APF at 0.1 s^{-1}, no obvious cracks can be seen at $\varepsilon_y = 0.03$. Failure begins in the middle layer at $\varepsilon_y = 0.07$ and continues in other layers. At $\varepsilon_y = 0.22$, the polymer is well contained within the structure and deformation is visible in all layers, showing a stable failure mode.

Stiffness, strength, and energy absorption obtained from stress-strain curves for strain rates of 0.1, 0.01, 0.001, 0.0005, and 0.00001 s^{-1} are shown in Fig. 10 (a)-(c), respectively. Two trials were performed for each strain rate. It is shown that stiffness increases with strain rate, but the three lowest rates result in similar stiffness values. Yield strength is consistent for three lowest strain rates but increases at higher strain rates. This indicates that low strain rates do not highly influence the mechanical behavior of APFs. Yield strength for the highest strain rate is over three times that of the lowest strain rate. This improved mechanical properties at high loading rates can be attributed to stiffer molecular chains that are reoriented within the base material [50]. Energy absorption is fairly consistent for all strain rates. This study provides a preliminary investigation into strain rate dependent mechanical performance of 3D printed structures.

4. Conclusions

We have demonstrated 3D printing and testing of novel architected foams with engineered mechanical performance. Increasing the relative density of the structure is inefficient for controlling stiffness, due to the bending-dominant behavior. The influence of the binder angle has been investigated as an alternative for tailoring the effective stiffness of the APF. Varying the binder size alters the stress transfer path of the structure, rendering the binder angle a more effective parameter for controlling stiffness. In addition to geometric parameters, the manufacturing
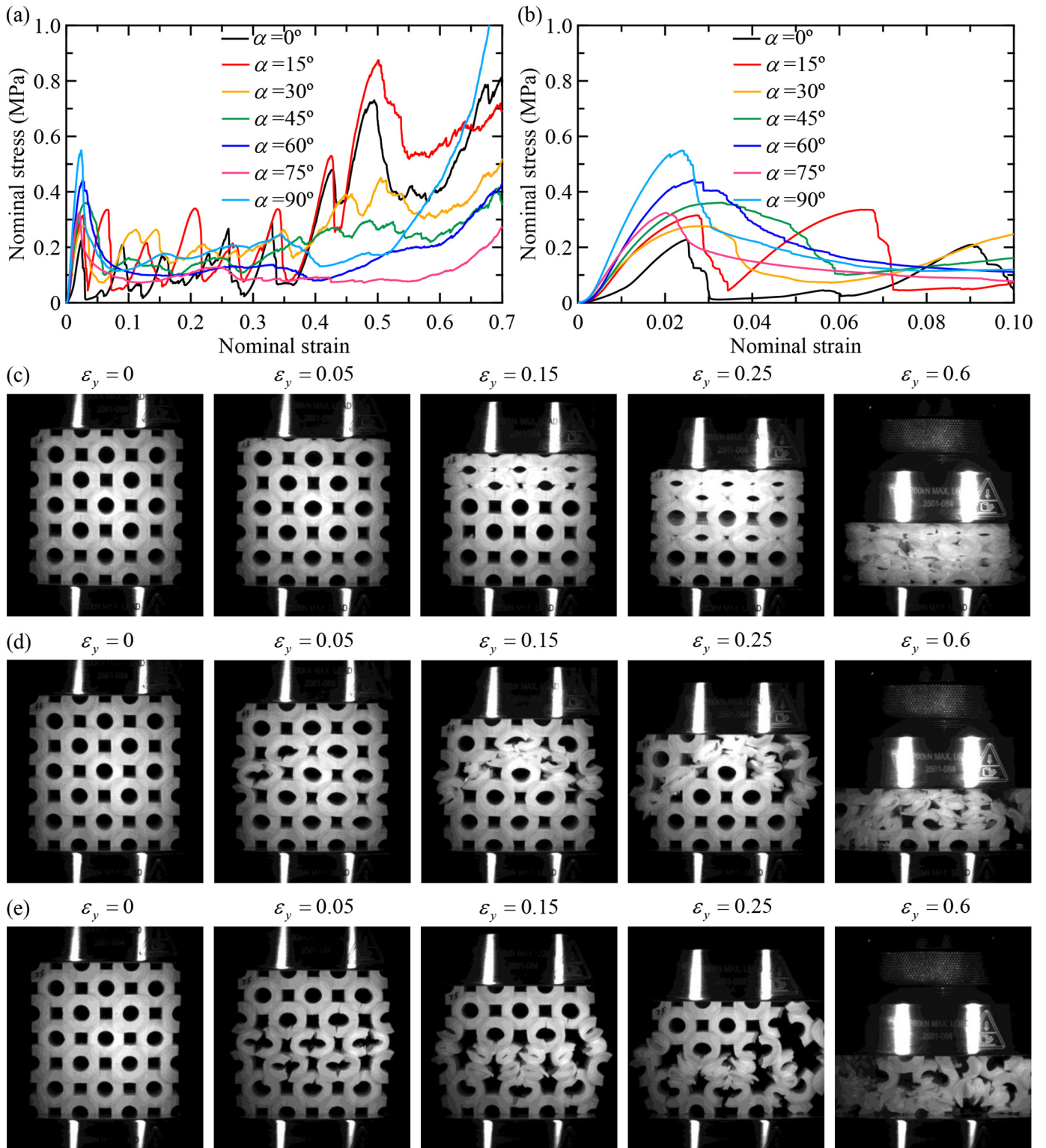
Fig. 7. Effect of printing direction on mechanical performance. (a)-(b) Stress-strain curves for different printing directions. (c)-(e) Deformation patterns for $\alpha = 15°$, $\alpha = 45°$, and $\alpha = 75°$, respectively.

process has a large impact on mechanical performance. Structure tends to fracture along the printing direction and mechanical properties are superior when loaded parallel to the printed layers. Moreover, the mechanical performance of APF is strain rate dependent due to the inherent rate sensitivity of the constitutive material. It should be pointed out that the strain rate tested here is still low, which cannot represent

all dynamic loading conditions. Extending the strain rate to higher levels will be essential to examine the feasibility to employ the proposed architected foams in blast and impact protection systems. In addition, the finite element simulations performed here cannot consider the layer-by-layer feature of the printed samples and manufacturing defects involved. This can be resolved by improving the current constitutive
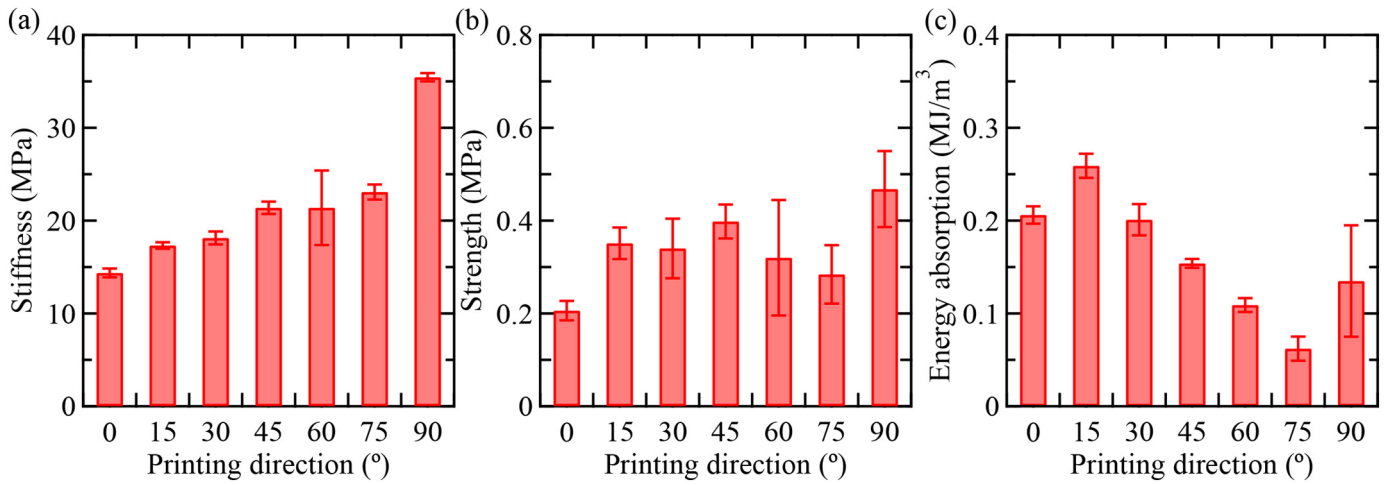
Fig. 8. Effect of printing direction on mechanical performance. (a) Stiffness as a function of α. (b) Strength as a function of α. (c) Energy absorption as a function of α. Here $a = 25mm$, $t/R = 1/10$, $r = 4t$, $\theta = 20°$.
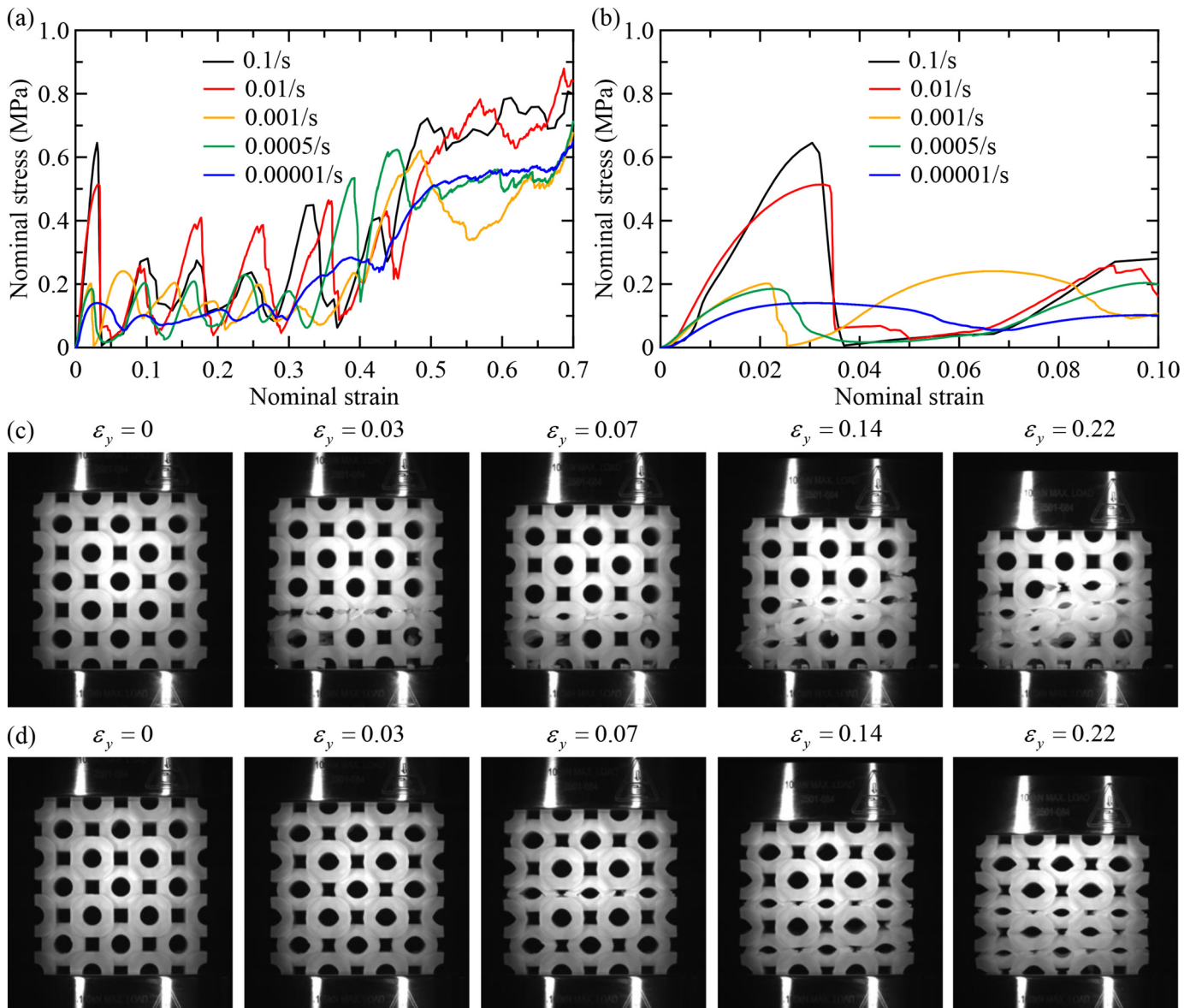
Fig. 9. Effect of loading rate from 10^{-5} to 0.1 s^{-1}. (a)-(b) Stress-strain curves for $\dot{\varepsilon} = 10^{-5}$, $\dot{\varepsilon} = 10^{-4}$, $\dot{\varepsilon} = 10^{-3}$, $\dot{\varepsilon} = 10^{-2}$, and $\dot{\varepsilon} = 10^{-1}$. (c) Deformation patterns for a strain rate of $\dot{\varepsilon} = 10^{-1}$, and (d) Deformation patterns for a strain rate of $\dot{\varepsilon} = 10^{-5}$. Here $a = 25mm$, $t/R = 1/10$, $r = 4t$, $\theta = 20°$.

Fig. 10. Effect of strain rate on mechanical performance. (a) Stiffness as a function of strain rate. (b) Strength as a function of strain rate. (c) Energy absorption as a function of strain rate. Here $a = 25$mm, $t/R = 1/10$, $r = 4t$, $\theta = 20^\circ$.
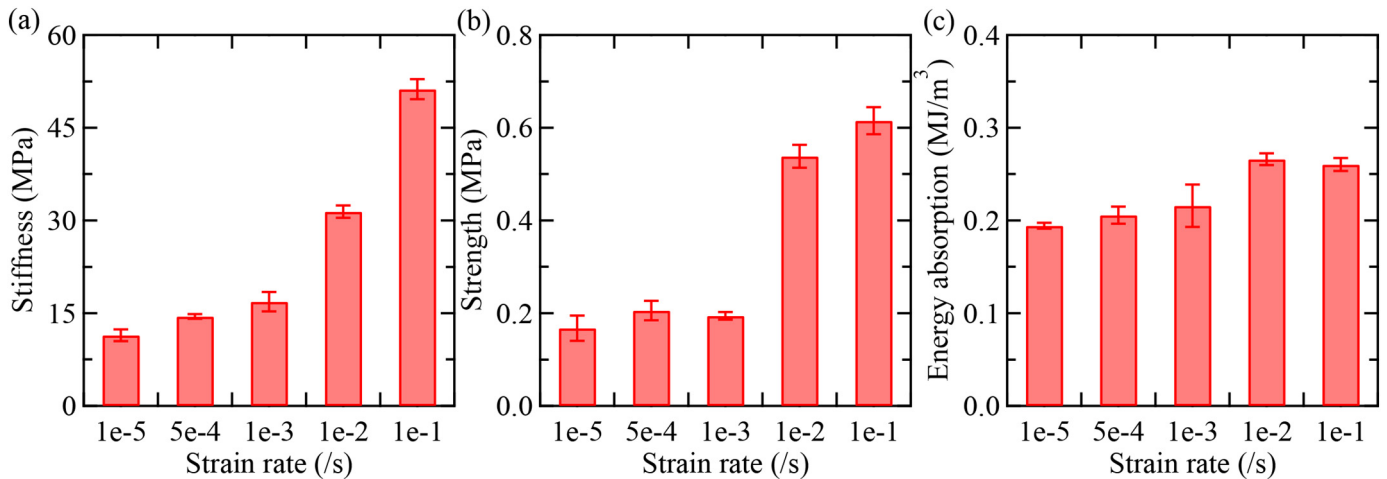
model to incorporate anisotropy and failure criteria. Nevertheless, the findings presented here can provide design guidelines for engineering architected foams to be employed within a wide range of applications, including structures of increased crashworthiness and composite sandwich panels with enhanced vibroimpact insulation and low-velocity impact resistance.

Data availability

The raw/processed data required to reproduce these findings cannot be shared at this time due to legal or ethical reasons. Data are however available from the authors upon reasonable request.

Author declaration

We wish to confirm that there are no known conflicts of interest associated with this publication and there has been no significant financial support for this work that could have influenced its outcome.

We confirm that the manuscript has been read and approved by all named authors and that there are no other persons who satisfied the criteria for authorship but are not listed. We further confirm that the order of authors listed in the manuscript has been approved by all of us.

We confirm that we have given due consideration to the protection of intellectual property associated with this work and that there are no impediments to publication, including the timing of publication, with respect to intellectual property. In so doing we confirm that we have followed the regulations of our institutions concerning intellectual property.

We understand that the Corresponding Author is the sole contact for the Editorial process (including Editorial Manager and direct communications with the office). He is responsible for communicating with the other authors about progress, submissions of revisions and final approval of proofs. We confirm that we have provided a current, correct email address which is accessible by the Corresponding Author and which has been configured to accepting email from yanyu.chen@louisville.edu

Declaration of Competing Interest

None.

Acknowledgments

References

[1] W.S. Sanders, L.J. Gibson, Mechanics of BCC and FCC hollow-sphere foams, Mater. Sci. Eng. A 352 (1–2) (2003) 150–161.

[2] C. Bonatti, D. Mohr, Large deformation response of additively-manufactured FCC metamaterials: from octet truss lattices towards continuous shell mesostructures, Int. J. Plast. 92 (2017) 122–147.

[3] O. Caty, E. Maire, T. Douillard, P. Bertino, R. Dejaeger, R. Bouchet, Experimental determination of the macroscopic fatigue properties of metal hollow sphere structures, Mater. Lett. 63 (13–14) (2009) 1131–1134.

[4] T. Fiedler, A. Öchsner, On the anisotropy of adhesively bonded metallic hollow sphere structures, Scr. Mater. 58 (8) (2008) 695–698.

[5] K. Boomsma, D. Poulikakos, F. Zwick, Metal foams as compact high performance heat exchangers, Mech. Mater. 35 (12) (2003) 1161–1176.

[6] S.T. Hong, D.R. Herling, Open-cell aluminum foams filled with phase change materials as compact heat sinks, Scr. Mater. 55 (10) (2006) 887–890.

[7] W.S. Sanders, L.J. Gibson, Mechanics of hollow sphere foams, Mater. Sci. Eng. A 347 (1–2) (2003) 70–85.

[8] N.J. Mills, C. Fitzgerald, A. Gilchrist, R. Verdejo, Polymer foams for personal protection: cushions, shoes and helmets, Compos. Sci. Technol. 63 (16) (2003) 2389–2400.

[9] K. Ahuja, R. Gaeta Jr., K. Ahuja, R. Gaeta Jr., A new wide-band acoustic liner with high temperature capability, 3rd AIAA/CEAS Aeroacoustics Conference 1997, p. 1701 , https://arc.aiaa.org/doi/abs/10.2514/6.1997-1701.

[10] S. Babaee, P. Wang, K. Bertoldi, Three-dimensional adaptive soft phononic crystals, J. Appl. Phys. 117 (24) (2015).

[11] T. Bleistein, M. Reis, X. Cheng, C. Redenbach, S. Diebels, A. Jung, Multiscale microsphere modelling of open-cell metal foams enriched by statistical analysis of geometric parameters, Mech. Mater. 142 (2020) 103295.

[12] A.P. Roberts, E.J. Garboczi, Elastic moduli of model random three-dimensional closed-cell cellular solids, Acta Mater. 49 (2) (2001) 189–197.

[13] W.Y. Jang, W.Y. Hsieh, C.C. Miao, Y.C. Yen, Microstructure and mechanical properties of ALPORAS closed-cell aluminium foam, Mater. Charact. 107 (2015) 228–238.

[14] I. Jeon, T. Asahina, The effect of structural defects on the compressive behavior of closed-cell Al foam, Acta Mater. 53 (12) (2005) 3415–3423.

[15] M.A. Kader, M.A. Islam, M. Saadatfar, P.J. Hazell, A.D. Brown, S. Ahmed, J.P. Escobedo, Macro and micro collapse mechanisms of closed-cell aluminium foams during quasi-static compression, Mater. Des. 118 (2017) 11–21.

[16] W.S. Sanders, Mechanical Behavior of Closed-Cell and Hollow-Sphere Metallic Foams, 2002.

[17] O. Friedl, C. Motz, H. Peterlik, S. Puchegger, N. Reger, R. Pippan, Experimental investigation of mechanical properties of metallic hollow sphere structures, Metall. Mater. Trans. B Process Metall. Mater. Process. Sci. 39 (1) (2008) 135–146.

[18] R. Kumar, H. Jain, S. Sriram, A. Chaudhary, A. Khare, V.A.N. Ch, D.P. Mondal, Lightweight open cell aluminum foam for superior mechanical and electromagnetic interference shielding properties, Mater. Chem. Phys. 240 (2020) 122274.

[19] A.G. Mamalis, D.E. Manolakos, M.B. Ioannidis, D.G. Chronopoulos, P.K. Kostazos, On the crashworthiness of composite rectangular thin-walled tubes internally reinforced with aluminium or polymeric foams: experimental and numerical simulation, Compos. Struct. 89 (3) (2009) 416–423.

[20] O. Kesler, L.K. Crews, L.J. Gibson, Creep of sandwich beams with metallic foam cores, Mater. Sci. Eng. A 341 (1–2) (2003) 264–272.

[21] K. Li, X.-L. Gao, Micromechanical Modeling of Three-Dimensional Open-Cell Foams, Adv. Soft Matter Mech. Springer, Berlin, Heidelberg, 2012 213–258.

[22] K. Li, X.L. Gao, A.K. Roy, Micromechanical modeling of three-dimensional open-cell foams using the matrix method for spatial frames, Compos. B Eng. 36 (3) (2005) 249–262.

[23] S.T. Szyniszewski, B.H. Smith, J.F. Hajjar, B.W. Schafer, S.R. Arwade, The mechanical properties and modeling of a sintered hollow sphere steel foam, Mater. Des. 54 (2014) 1083–1094.

[24] A. Taşdemirci, Ç. Ergönenç, M. Güden, Split Hopkinson pressure bar multiple reloading and modeling of a 316 L stainless steel metallic hollow sphere structure, Int. J. Impact Eng. 37 (3) (2010) 250–259.

[25] T. Fiedler, C. Veyhl, I.V. Belova, T. Bernthaler, B. Heine, G.E. Murch, Mechanical properties and micro-deformation of sintered metallic hollow sphere structure, Comput. Mater. Sci. 74 (2013) 143–147.

[26] A. Sutygina, U. Betke, M. Scheffler, Open-cell aluminum foams by the sponge replication technique: a starting powder particle study, Adv. Eng. Mater. 12 (23) (2020) 3840.

[27] P. Lhuissier, A. Fallet, L. Salvo, Y. Brechet, Quasistatic mechanical behaviour of stainless steel hollow sphere foam: macroscopic properties and damage mechanisms followed by X-ray tomography, Mater. Lett. 63 (13–14) (2009) 1113–1116.

[28] M. Xu, Z. Xu, Z. Zhang, H. Lei, Y. Bai, D. Fang, Mechanical properties and energy absorption capability of AuxHex structure under in-plane compression: theoretical and experimental studies, Int. J. Mech. Sci. 159 (2019) 43–57.

[29] H. Jia, H. Lei, P. Wang, J. Meng, C. Li, H. Zhou, X. Zhang, D. Fang, An experimental and numerical investigation of compressive response of designed Schwarz Primitive triply periodic minimal surface with non-uniform shell thickness, Extrem. Mech. Lett. 37 (2020).

[30] K. Pajunen, P. Johanns, R.K. Pal, J.J. Rimoli, C. Daraio, Design and impact response of 3D-printable tensegrity-inspired structures, Mater. Des. 182 (2019) 1–9.

[31] J. Xu, Y. Wu, L. Wang, J. Li, Y. Yang, Y. Tian, Z. Gong, P. Zhang, S. Nutt, S. Yin, Compressive properties of hollow lattice truss reinforced honeycombs (Honeytubes) by additive manufacturing: patterning and tube alignment effects, Mater. Des. 156 (2018) 446–457.

[32] F. Usta, F. Scarpa, H.S. Türkmen, Edgewise compression of novel hexagonal hierarchical and asymmetric unit cells honeycomb metamaterials, Mater. Today Commun. 24 (2020) 101102.

[33] S. Hou, T. Li, Z. Jia, L. Wang, Mechanical properties of sandwich composites with 3d-printed auxetic and non-auxetic lattice cores under low velocity impact, Mater. Des. 160 (2018) 1305–1321.

[34] H. Yang, B. Wang, L. Ma, Designing hierarchical metamaterials by topology analysis with tailored Poisson's ratio and Young's modulus, Compos. Struct. 214 (2019) 359–378.

[35] M. Kaur, T.G. Yun, S.M. Han, E.L. Thomas, W.S. Kim, 3D printed stretching-dominated micro-trusses, Mater. Des. 134 (2017) 272–280.

[36] Z. Vangelatos, K. Komvopoulos, J. Spanos, M. Farsari, C. Grigoropoulos, Anisotropic and curved lattice members enhance the structural integrity and mechanical performance of architected metamaterials, Int. J. Solids Struct. 193–194 (2020) 287–301.

[37] Y. Wang, B. Ramirez, K. Carpenter, C. Naify, D.C. Hofmann, C. Daraio, Architected lattices with adaptive energy absorption, Extrem. Mech. Lett. 33 (2019) 1–6.

[38] O. McGee, H. Jiang, F. Qian, Z. Jia, L. Wang, H. Meng, D. Chronopoulos, Y. Chen, L. Zuo, 3D printed architected hollow sphere foams with low-frequency phononic band gaps, Addit. Manuf. 30 (2019) 100842.

[39] H. Jiang, Y. Chen, Lightweight architected hollow sphere foams for simultaneous noise and vibration control, J. Phys. D. Appl. Phys. 52 (32) (2019) 325303.

[40] M. Mohsenizadeh, F. Gasbarri, M. Munther, A. Beheshti, K. Davami, Additively-manufactured lightweight Metamaterials for energy absorption, Mater. Des. 139 (2018) 521–530.

[41] M.G. Tarantino, O. Zerhouni, K. Danas, Random 3D-printed isotropic composites with high volume fraction of pore-like polydisperse inclusions and near-optimal elastic stiffness, Acta Mater. 175 (2019) 331–340.

[42] S. Kramer, J.L. Jordan, H. Jin, J. Carroll, A.M. Beese, Mechanics of Additive and Advanced Manufacturing, Volume 8: Proceedings of the 2018 Annual Conference on Experimental and Applied Mechanics, Springer, 2018.

[43] Instron, Instron 5569 Load Frame Manual, DOI, 2008.

[44] P. Zhang, A.C. To, Transversely isotropic hyperelastic-viscoplastic model for glassy polymers with application to additive manufactured photopolymers, Int. J. Plast. 80 (2016) 56–74.

[45] L. Liu, A Triaxiality-Dependent Constitutive Model for Predicting Damage-Induced Softening in 3D- Printed Soft Suture Layer, 2018.

[46] E.M. Arruda, M.C. Boyce, A Three-Dimensional Constitutive Model for the Large Stretch Behavior of Rubber Elastic Materials, 1993.

[47] Abaqus 6.14 Documentation, Dassault Systems Simulia Corp, 2014.

[48] Y. Duan, B. Du, X. Shi, B. Hou, Y. Li, Quasi-static and dynamic compressive properties and deformation mechanisms of 3D printed polymeric cellular structures with kelvin cells, Int. J. Impact Eng. 132 (2019) 103303.

[49] C.W. Visser, D.N. Amato, J. Mueller, J.A. Lewis, Architected polymer foams via direct bubble writing, Adv. Mater. 31 (2019) 1–8.

[50] M.C. Boyce, D.M. Parks, A.S. Argon, Large inelastic deformation of glassy polymers. part I: rate dependent constitutive model, Mech. Mater. 7 (1) (1988) 15–33.